

Semi-Automatic Discrimination of Normal Tissue and Liver Cancer Lesions in Contrast Enhanced X-Ray CT-Scans [★]

Sanat Upadhyay¹, Manos Papadakis¹, Saurabh Jain², Gregory Gladish MD³, Ioannis A. Kakadiaris⁴, and Robert Azencott¹

¹ Department of Mathematics, University of Houston, TX, USA

² Center for Imaging Sciences, John Hopkins University, MD, USA

³ MD Anderson Cancer Center, The University of Texas, TX, USA

⁴ Department of Computer Science, University of Houston, TX, USA

Abstract. In this paper we present a set of 3D-rigid motion invariant texture features. We experimentally establish that when they are combined with mean attenuation intensity differences the new augmented features are capable of discriminating normal from abnormal liver tissue in arterial phase contrast enhanced X-ray CT-scans with high sensitivity and specificity. To extract these features CT-scans are processed in their native dimensionality. We experimentally observe that the 3D-rotational invariance of the proposed features improves the clustering of the feature vectors extracted from normal liver tissue samples.

Keywords: Liver cancer, 3D-Texture classification, Rotationally invariant features, Soft tissue discrimination.

1 Introduction and Previous work

The early detection of liver cancer lesions can potentially improve the management of various forms of liver cancer. Typically, liver lesions are identified using contrast enhanced CT scans acquired at different phases of perfusion of the hepatic parenchyma by the infused contrast agent. The task of identifying the lesions is performed by a radiologist using a large number of images generated from this multiphase CT acquisition and requires significant time and effort.

In this work, we present an algorithm and experimental results that demonstrate the feasibility of the development of a semi-automatic screening tool capable of detecting liver abnormalities in contrast enhanced x-ray CT-scans. Specifically, utilizing ideas proposed by Jain *et. al.* [1] we develop 3D-rigid motion invariant texture features. We experimentally establish that when these features are combined with mean attenuation intensity differences the new augmented features are capable of discriminating normal from abnormal liver tissue in arterial phase contrast enhanced X-ray CT-scans with high sensitivity and specificity.

[★] This work was partially supported by NSF DMS 0915242 award.

When scans are acquired during different perfusion phases of the contrast agent, liver lesions result in hypodense or hyperdense Regions of Interest (ROI) relative to normal hepatic parenchyma. Quite often, in the arterial phase hypodense ROIs are adjacent to hyperdense ones due to the increased vascularization of active cancerous lesions. The driving assumption in our approach is that liver tissue ROIs can be represented in a contrast-enhanced x-ray CT scan by two components, *3D-texture* and *local mean intensities*. The first of the two components captures the structure while the second provides the average intensity of the ROI, which is a traditional feature for tissue discrimination and is much more observable by the eye of the trained beholder than the former. We demonstrate though that local attenuation intensity averages are not by themselves robust enough to discriminate normal from abnormal tissue. Our results reveal that features capturing the structural characteristics of the 3D-textures associated with these tissue types in general perform better than the former, or at least equally well.

Texture-based lesion segmentation has been successfully used in the past for the detection of cancerous hepatic lesions [2]. In contrast to the herein proposed method, which is natively implemented in 3D, proposed texture features in the existing literature are extracted in a slice by slice manner by combining first and second order moments [3]. Very similar approaches have also been used to segment the liver from neighboring organs [4–6]. Apart from the fact that our methods are natively designed to work in 3D, a fundamental difference between previous texture-based approaches and our work is that they use significantly more complex classifiers. Liver segmentation and detection of cancerous lesions has been mostly performed with non-texture based methods as in [7–12] where the difference in attenuation intensity between more and less contrast-perfused ROIs is used for feature extraction or as in [13, 14] where deformable models are utilized to generate the boundaries between normal and abnormal tissues. However, both of these approaches mostly limit the detection of cancer lesions to the hypodense ones, because differences in average intensities are typically the dominant discriminative features.

In spite of the significant successes in the field of hepatic tumor detection and segmentation, our work opens an unexplored direction. The novelty of our approach relies first, on the use of 3D isotropic multiscale analysis for the extraction of 3D-rigid motion invariant texture features; second, on augmenting these texture features with attenuation intensity-based features. The proposed 3D-rigid motion invariant features allow feature vectors from normal tissue samples to form clusters that are more well-defined than the clusters formed when the 3D-texture features do not account for 3D-rotations. This enhances the discriminatory power of the proposed features (Fig. 3). Our experimental results are not directly comparable with the results of others, because we only test the discriminative power of our features on sets of ROIs and we don't segment normal from abnormal liver tissue. However, it appears that the proposed features can be used for tissue discrimination with high sensitivity and specificity rates rendering them as a promising tool for developing segmentation algorithms.

2 Methods

Our tissue classification scheme consists of two levels of classifiers. The design of both levels is traditional. The first level consists of an ensemble of SVMs classifiers which at the second level decide by majority voting whether a tissue ROI is normal or abnormal. The SVM classifiers use low-dimensional feature vectors whose components express the statistical disparity at one or more scales of the 3D-texture corresponding to a given liver tissue ROI for the 3D-texture of a normal reference ROI and the difference of average intensities between the two ROIs. To develop these classifiers the human operator selects a small number of reference normal ROIs from an x-ray CT-scan that is examined. The proposed feature design takes into account that a liver consists of soft tissues with varying 3D-orientations thus requiring features to be invariant under 3D-rotations and translations. In particular, cancer will tend to develop along blood vessels, which themselves appear with a varying degree of 3D-orientations. Moreover, malignancies form their vasculature with an even richer orientation variation in 3D. Attenuation intensity local average-based features would automatically be invariant to 3D-rigid motions, and therefore insensitive to the variety of 3D-orientations of the patterns formed by tissues of interest, but 3D-texture features must be specifically designed to be 3D-rigid motion invariant. We discuss the details of this design in the next paragraph.

2.1 3D-Texture Based Features

To discriminate 3D-textures corresponding to soft-tissue ROIs we assume that both ROIs have zero mean. The texture component of the proposed features is derived by combining 3D-rigid motion invariant monoscale ‘distances’ between texture signatures derived by fitting order-one Gaussian Markov Random Field (GMRF) models to the orbits of 3D-texture rotations corresponding to the zero-mean tissue ROIs, as proposed in [1, 15]. In this manner, our features quantify 3D-texture disparities at various scales. A 3D-texture \mathbf{X} is modeled as a spatially homogeneous random field defined on the continuous domain \mathbb{R}^3 . Image acquisition generates the realization of \mathbf{X} in the form of a digital 3D-image whose values at the points of a discrete sampling lattice Λ are the exact same values of its ‘continuous parent’ at the grid points of Λ . Hence, an α -rotation of the discrete texture \mathbf{X} is the restriction of the α -rotation of its continuous parent on Λ . So, rotating the discrete texture \mathbf{X} amounts to rotating the autocovariance ρ of its continuous parent.

Using the approximation of ρ by the empirical autocovariance function ρ_0 we ‘fit’ a very simple order-one GMRF model to the data $\rho_0(\mathbf{k})_{\mathbf{k} \in \Lambda}$ from which the autocovariance matrix of the fitted model $\hat{\Sigma}$ and its inverse $(\hat{\Sigma})^{-1}$ are computed following a method originally proposed in [16] adopted for 3D in [1, 17]. By taking any α -rotation of ρ_0 and fitting the same model to the rotated $\rho_0(\hat{\Sigma})\alpha$ is obtained. Since, 3D-shifts induced by the action of Λ do not affect the discrete texture \mathbf{X} , due to the spatial homogeneity assumption it follows that the orbit $\Gamma_{\mathbf{X}}(\alpha) = (\hat{\Sigma})\alpha$, $\alpha \in SO(3)$ is the *monoscale 3D-rigid motion covariant texture*

signature of the observed texture \mathbf{X} at the scale corresponding to the density of the lattice Λ . This led Jain *et al* [1] to propose a 3D-rigid motion invariant texture ‘distance’ at this scale

$$Rdist(\mathbf{X}, \mathbf{Y}) := \min_{\tau \in SO(3)} \int_{SO(3)} \text{KLdist}(\Gamma_{\mathbf{X}}(\alpha), \Gamma_{\mathbf{Y}}(\tau\alpha)) d\alpha, \quad (1)$$

where $\text{KLdist}(\Sigma_1, \Sigma_2) = \frac{1}{2} \text{Trace}(\Sigma_2^{-1}\Sigma_1 + \Sigma_1^{-1}\Sigma_2 - 2I_{N \times N})$. We stress that the 3D-texture corresponding to a tissue ROI is almost never an order one GMRF. Yet, we carry out our computations as if it were such a GMRF. We use this computationally simple and numerically efficient stochastic model as a probe for tissue discrimination and not as a texture model for soft tissues. The 3D-texture features for the promised liver tissue SVM classifiers are constructed via (1).

2.2 Feature Extraction

Let $\{\mathbf{s}_k\}_{k=1,2,\dots,N}$ be 3D volumes from normal or abnormal liver tissues and $\mathbf{\Lambda}_k := \mathbf{s}_k \cap \Lambda$. Now, fix a sample \mathbf{n} which is known to be normal to be the *reference normal*. For each one of the $\{\mathbf{s}_k\}_{k=1,2,\dots,N}$ we derive the feature vector $\mathbf{f}(\mathbf{s}_k; \mathbf{n})$ relative to \mathbf{n} according to the following algorithm.

The first component of the feature vector $\mathbf{f}(\mathbf{s}_k; \mathbf{n})$ is

$$D_M(\mathbf{s}_k, \mathbf{n}) := \frac{|\bar{\mathbf{s}}_k - \bar{\mathbf{n}}|}{\sqrt{\text{var}(\mathbf{s}_k) + \text{var}(\mathbf{n})}}.$$

D_M standardizes the statistical disparity due to the difference in the average attenuation intensity between \mathbf{s}_k and \mathbf{n} . To form the remaining components of the feature vector $\mathbf{f}(\mathbf{s}_k; \mathbf{n})$, we use the 3D-rigid motion invariant statistical disparity $RD_j(\mathbf{s}_k, \mathbf{n})$ at scales $j = 0, -1$, between the 3D textures corresponding to \mathbf{s}_k and \mathbf{n} where

$$RD_j(\mathbf{s}_k, \mathbf{n}) = \max \left\{ 0, \frac{Rdist_j(\mathbf{s}_k, \mathbf{n}) - \text{diam}_{\mathbf{n}}(j)}{\text{diam}_{\mathbf{n}}(j)} \right\}. \quad (2)$$

[1]. If for a given sample \mathbf{s}_k and at some scale j , $RD_j(\mathbf{s}_k, \mathbf{n})$ is large, then we can conclude that the sample \mathbf{s}_k has a different 3D texture than the reference normal \mathbf{n} \mathbf{s}_k thus more the tissue from which \mathbf{s}_k originated is likely to be abnormal. To compute $RD_j(\mathbf{s}_k, \mathbf{n})$ we make some non-trivial modifications to the algorithm proposed in [15] to make it applicable to ROIs that are not 3D cubes. We describe those modifications below:

Computation of $RD_j(\mathbf{s}_k, \mathbf{n})$: (i) Adjust intensity values in both \mathbf{s}_k and \mathbf{n} to have zero mean.

(ii) Upsample each \mathbf{s}_k to a twice the denser grid as in [15]. The upsampled 3D-texture sample is convolved with the isotropic low-pass synthesis filter H_0 :

$$H_0(\xi) = \begin{cases} 1 & |\xi| \leq \frac{1-\beta}{2\tau}, \\ \frac{1}{2} \left[1 + \cos \left(\frac{\pi\tau}{\beta} \left(|\xi| - \frac{1-\beta}{2\tau} \right) \right) \right] \frac{1-\beta}{2\tau} & \frac{1-\beta}{2\tau} < |\xi| \leq \frac{1+\beta}{2\tau}, \\ 0 & \text{otherwise,} \end{cases} \quad (3)$$

where $\tau = 100/84$ and $\beta = 1/7$. The isotropy of H_0 increases the accuracy of the computation of ρ_0 .

(iii) Let \mathbf{t} be a node in \mathbf{s}_k , then a *neighborhood* of \mathbf{t} is $\eta_{\mathbf{t}} := (\mathbf{t} + W) \subset \Lambda_k$ where W is a symmetric neighborhood of the origin. We set $W = W^+ \cup W^-$ where $W^- = -W^+$ and $W^+ = \{(2^{-j+1}, 0, 0), (0, 2^{-j+1}, 0), (0, 0, 2^{-j+1})\}$. The order-one GMRF model limits interactions within W . Also define $\Lambda'_k \subset \Lambda_k$ to satisfy $(\eta_{\mathbf{t}} + W) \subset \Lambda_k$ for every $\mathbf{t} \in \Lambda'_k$. We extract our statistics from $\mathbf{s}_k|_{\Lambda'_k}$.

(iv) Compute the empirical auto-covariance matrix ρ_0 of $\mathbf{s}_k|_{\Lambda'_k}$ via:

$$\rho_0(\mathbf{t}) = \frac{1}{|\Lambda'_k|} \sum_{\mathbf{r} \in \Lambda'_k} s_{k_{\mathbf{r}}} s_{k_{\mathbf{r}+\mathbf{t}}}, \quad \text{for all } \mathbf{t} \text{ such that } \|\mathbf{t}\|_{\infty} \leq 2^{-j+2}.$$

where $|\Lambda'_k|$ denotes the number of voxels in Λ'_k ; ρ_0 is of size $(2^{-j+3} + 1)^3$.

(v) Any of the 3D textures need not satisfy $\rho_0(\mathbf{t}) = \rho_0(-\mathbf{t})$. So we artificially symmetrize ρ'_0 by setting $\rho'_0(\mathbf{t}) := \frac{1}{2} [\rho_0(\mathbf{t}) + \rho_0(-\mathbf{t})]$ for all $\mathbf{t} \in \Lambda'_k$ such that $\|\mathbf{t}\|_{\infty} \leq 2^{-j+2}$. To simplify the notation from now on we use $\rho'_0 = \rho_0$.

(vi) Let $\mathbf{y}_{\mathbf{r}} = [s_{k_{\mathbf{l}}} + s_{k_{-\mathbf{l}}}]$, $\mathbf{l} \in (\mathbf{r} + W^+)$. Define $\mathbf{Y} = [\mathbf{y}_{\mathbf{r}}]$, $\mathbf{r} \in \Lambda'_k$. The least squares estimates $\hat{\sigma}$ and $\hat{\boldsymbol{\theta}}$ of the order-one GMRF model that fits the data are given by the statistics: $\hat{\boldsymbol{\theta}}(\mathbf{s}_k) = (\mathbf{Y}^T \mathbf{Y})^{-1} \mathbf{Y}^T \mathbf{s}_k$ and $\hat{\sigma}^2(\mathbf{s}_k) = \frac{1}{|\Lambda'_k|} \left(\mathbf{s}_k^T \mathbf{s}_k - \hat{\boldsymbol{\theta}}^T \mathbf{Y}^T \mathbf{s}_k \right)$

(vii) $Y^T \mathbf{s}_k$ and $Y^T Y$ are given by $(\mathbf{Y}^T \mathbf{s}_k)_{\mathbf{r}} = |\Lambda'_k| (\rho_0(\mathbf{r}) + \rho_0(-\mathbf{r})) \quad \forall \mathbf{r} \in W^+$

$(\mathbf{Y}^T \mathbf{Y})_{(\mathbf{t}, \mathbf{r})} = |\Lambda'_k| [\rho_0(\mathbf{r}-\mathbf{t}) + \rho_0(\mathbf{r}+\mathbf{t}) + \rho_0(-\mathbf{r}-\mathbf{t}) + \rho_0(-\mathbf{r}+\mathbf{t})] \quad (\mathbf{t}, \mathbf{r}) \in W^+ \times W^+$.

(viii) The computation of $(Y^T Y)^{-1}$ is performed as in [15].

By iterating for a finite set of rotations the previous steps the rotationally covariant signatures $\Gamma_{\mathbf{s}_k}$ and $\Gamma_{\mathbf{n}}$ are generated as in [1] and finally $RD_j(\mathbf{s}_k, \mathbf{n})$ is computed for $j = 0, -1$ using the isotropic low pass filter [1] with $\tau = \frac{2^{-j} \cdot 100}{84}$. We keep the low-pass output at the original resolution. To extract the order-one GMRF statistics we use the interactions of pixels 2^{-j+1} apart and we repeat all of the previous steps with the exception of step (ii). As noted in [1] observing textures at lower scales compensates for the loss of the tissue textures information due the use of the order-one GMRF model.

3 Experiments and Results

Arterial phase X-ray CT scans of liver from six patients were obtained. All scans were obtained with almost cubic voxels which is necessary for our method. From each of the six CT-scan series, we selected a set of eight normal and twelve abnormal ROIs, chosen by an expert radiologist. The abnormal ROIs contained one or more cancer lesions at different stages of maturity and size. For each of the series we perform three experiments. First, we use each one of the normal ROIs \mathbf{n} , as a *reference normal*. Then, we compute three sets of feature vectors. Using the feature vectors we develop a two class SVM-classifier corresponding to \mathbf{n} with each one of these sets of features. The kernel of the SVM-classifier is approximated by Radial Basis functions and for our implementation we use the free package LibSVM. Next we define the three said types of features.

(a) $\mathbf{f}_1(\mathbf{s}_k) = (D_M(\mathbf{s}_k, \mathbf{n}))$, classifies samples \mathbf{s}_k by exclusively using differences of ROI mean attenuation intensities.

(b) $\mathbf{f}_2(\mathbf{s}_k) = (RD_0(\mathbf{s}_k, \mathbf{n}), RD_{-1}(\mathbf{s}_k, \mathbf{n}))$, classifies samples \mathbf{s}_k using their 3D-texture disparities at the original scale and at one scale coarser than the original. 3D-displacements and 3D-rotations of ROIs do not influence the statistical disparity of the textures of any two ROIs. Any directional characteristics native to each texture contribute to this texture disparity feature only with respect to their relative 3D-orientations.

(c) $\mathbf{f}_3(\mathbf{s}_k) = (RD_0(\mathbf{s}_k, \mathbf{n}), RD_{-1}(\mathbf{s}_k, \mathbf{n}), D_M(\mathbf{s}_k, \mathbf{n}))$ combines multiscale texture disparity with differences in average attenuation intensity.

To validate the performance of each set of the features above, we test each of the SVM-classifiers associated with a normal tissue ROI using only this set of features. We also test a classifier combining input from each one of these classifiers by majority voting referred to as *SVM-voting* separately for features \mathbf{f}_1 , \mathbf{f}_2 and \mathbf{f}_3 . We estimate the accuracy of these classifiers in two ways.

Experiment 1: We randomly divide 20 samples in two groups, with 4 normal and 6 abnormal ROIs in each group. We perform a *two fold cross validation* by alternately training the SVM classifier on each group and testing it on the other. The average accuracy of each pair of classifiers is referred to as the accuracy of the two-fold classification. We repeat the previous test 100 times. The average accuracy of the two-fold classification from these 100 random trials is shown in Tables 1, 2. The average accuracy of the SVM-voting classifier for the same 100 random trials is also shown in Tables 1 and 2.

Experiment 2: This leave-two-out experiment essentially assesses the generalization capacity of the proposed classifiers. From the sample of twenty tissues from each patient we use 18 of them for training and two for testing. Leave-two-out accuracy is calculated for each of the eight SVM classifiers corresponding to each of the normal ROIs for each of the CT-scan series and for each of the proposed features \mathbf{f}_1 , \mathbf{f}_2 and \mathbf{f}_3 . We also assess the performance of the SVM-voting classifier. In the same way Tables 1 and 2 provide the average performance of these classifiers tested on all possible 96 partitions of the ROI set from each CT-scan series.

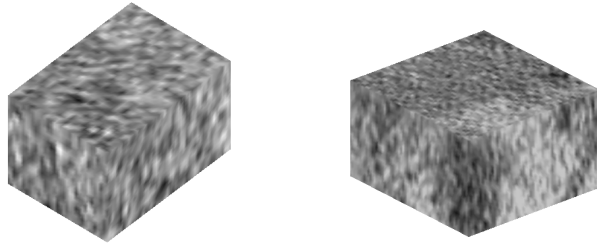


Fig. 1. Typical 3D-view of the texture of a normal liver ROI (left) and of an abnormal (neoplastic) liver ROI (right).

	Reference Normal	Two fold cross-validation			Leave-two-out-validation		
		Features used			Features used		
		D_M	(RD_0, RD_{-1})	(RD_0, RD_{-1}, D_M)	D_M	(RD_0, RD_{-1})	(RD_0, RD_{-1}, D_M)
L1	N1	95.0	94.4	100	92.7	80.7	100
	N2	75.8	90.4	97.7	77.6	84.4	100
	N3	77.0	91.6	98.1	71.4	90.1	100
	N4	95.6	95.1	97.8	100	91.1	100
	N5	94.9	95.1	98.1	99.5	93.8	100
	N6	94.9	94.4	99.2	99.5	89.6	100
	N7	95.5	92.8	99.1	100	90.6	100
	N8	95.2	95.0	97.9	100	95.8	100
	Average	90.5	93.6	98.5	92.6	89.5	100
<i>SVM-Voting</i>	94.8	94.0	98.6	100	89.1	100	
L2	N1	90.3	91.0	99.2	78.1	79.2	100
	N2	92.3	79.5	99.4	95.8	95.8	100
	N3	91.1	91.3	99.7	86.5	87.0	100
	N4	92.0	88.6	99.4	90.6	86.5	100
	N5	92.2	89.0	98.5	75.0	81.8	100
	N6	92.3	84.5	96.4	81.3	92.2	99.5
	N7	85.4	93.5	99.6	69.3	91.1	100
	N8	88.9	91.2	98.4	88.0	87.0	100
	Average	90.5	88.6	98.8	83.1	87.6	99.9
<i>SVM-Voting</i>	91.2	90.2	99.7	80.2	87.0	100	

Table 1. The entries of the table denotes the accuracy in percentage for each set of proposed features. SVM Classifiers are defined for each set of features and relative to each of the normal ROIs in each CT-scan series of Livers from 2 patients (L1, L2). Then we observe the average accuracy obtained from N1 to N8. *SVM-Voting* gives the classification based on the majority voting of *reference normals* used for training

4 Discussion

In this paper we present a novel set of features combining information of multi-scale texture disparity with the difference between average attenuation values for a given pair of texture patches one of which corresponds to normal tissue. These features exploit the full power of the 3D information modern scanners provide. We develop our features and the associated SVM classifiers using normal tissue reference ROIs only, because this type of tissue is less diverse within the same organ. Since the proposed disparities between normal tissues are also typically relatively small, because not absolute but only relative 3D-orientations of directional characteristics influence the evaluation of textural disparities (Fig. 3) making disparity assessments obtained from different SVM classifiers to agree. Tables 1, 2 support this claim by manifesting the robust assessment of textural similarity between normal tissues and the dissimilarity between normal and abnormal ones enabling thus a highly accurate SVM voting classification.

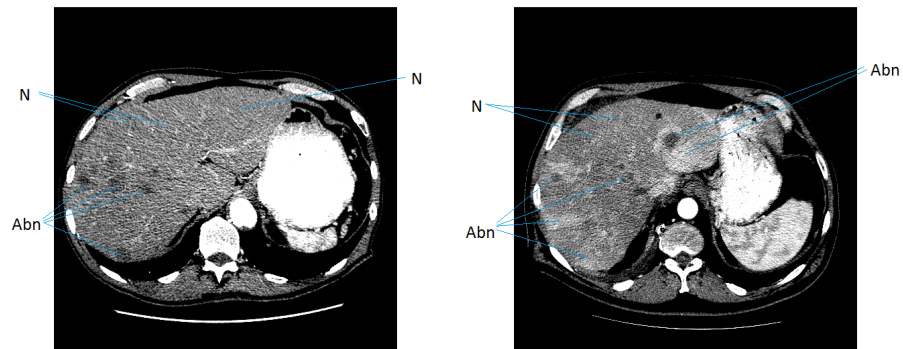


Fig. 2. Examples of our choices of normal (N) and diseased (Abn) regions, whose cross-sections are shown on 2D slices. We selected many different kind of abnormalities for our experiments, which includes tumors of different sizes and from different stages

References

1. Jain, S., Papadakis, M., Upadhyay, S., Azencott, R.: Rigid-motion-invariant classification of 3-D textures. *IEEE Transactions on Image Processing* **21**(5) (2012) 2449–2463
2. Pescia, D., Paragios, N., Chemouny, S.: Automatic detection of liver tumors. In: 5th IEEE International Symposium on Biomedical Imaging: From Nano to Macro. (2008) 672–675
3. Haralick, R.M., Shanmugam, K., Dinstein, I.: Textural features for image classification. *IEEE Transactions on Systems, Man and Cybernetics* **SMC-3**(6) (nov. 1973) 610–621
4. Liu, J., Hu, Q., Chen, Z., Heng, P.: Adaptive liver segmentation from multi-slice CT scans. In Peng, Y., Weng, X., Magjarevic, R., eds.: 7th Asian-Pacific Conference on Medical and Biological Engineering. Volume 19 of IFMBE Proceedings., Springer Berlin Heidelberg (2008) 381–384
5. Susomboon, R., Raicu, D., Furst, J., Johnson, T.: A co-occurrence texture semi-invariance to direction, distance and patient size. In Reinhardt, J., Pluim, J., eds.: *Proc. Medical Imaging 2008: Image Processing*. Volume 6914., SPIE (2008)
6. Pham, M., Susomboon, R., Disney, T., Raicu, D., Furst, J.: A comparison of texture models for automatic liver segmentation. In Pluim, J.P.W., Reinhardt, J.M., eds.: *Proc. Medical Imaging 2007: Image Processing*. Volume 6512., SPIE (2007)
7. Abdel-massieh, N., Hadhoud, M., Amin, K.: Automatic liver tumor segmentation from ct scans with knowledge-based constraints. In: 5th Cairo International Biomedical Engineering Conference, Cairo International Biomedical Engineering Conference, IEEE (December 2010) 215–218
8. Militzer, A., Hager, T., Ja andger, F., Tietjen, C., Hornegger, J.: Automatic detection and segmentation of focal liver lesions in contrast enhanced CT images. In: 20th International Conference on Pattern Recognition. (aug. 2010) 2524–2527

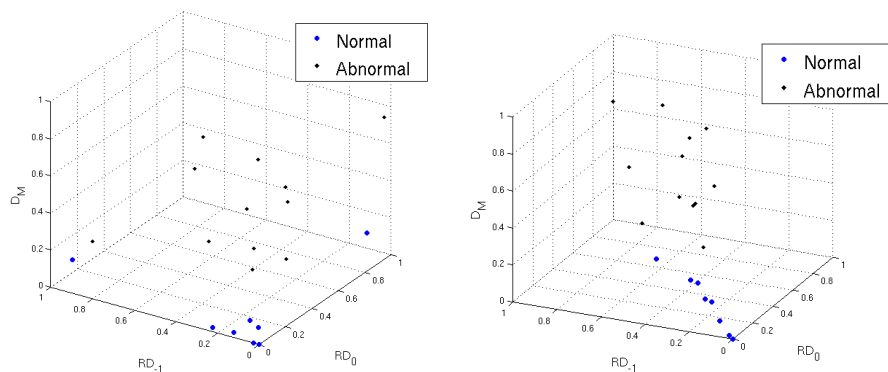


Fig. 3. Scatterplots show that the use of 3D-rotationally invariance texture disparities improves normal tissue ROI feature vector clustering. Left: RD_j 's given by texture distance $Rdist_j$ (Eq. (1)). Most feature vectors from normal tissue ROIs cluster around the origin and clearly away from their abnormal ROI counterparts. Right: Texture disparities are computed using $KLdist$ only, without averaging over 3D rotations. The normal tissue ROI cluster is less pronounced and it is more proximal to abnormal tissue ROI feature vectors.

9. Massoptier, L., Casciaro, S.: A new fully automatic and robust algorithm for fast segmentation of liver tissue and tumors from CT scans. Volume 18., Springer Berlin / Heidelberg (2008) 1658–1665
10. Zhou, J., Xiong, W., Tian, Q., Qi, Y., Liu, J., Leow, W., Han, T., Venkatesh, S., Wang, S.: Semi-automatic segmentation of 3d liver tumors from CT scans using voxel classification and propagational learning. MIDAS (2008)
11. Seo, K.: Automatic hepatic tumor segmentation using composite hypotheses. In Kamel, M., Campilho, A., eds.: Image Analysis and Recognition. Volume 3656 of Lecture Notes in Computer Science., Springer Berlin / Heidelberg (2005) 922–929
12. Park, S., Seo, K., Park, J.: Automatic hepatic tumor segmentation using statistical optimal threshold. In Sunderam, V., van Albada, G., Sloot, P., Dongarra, J., eds.: Computational Science ICCS 2005. Volume 3514 of Lecture Notes in Computer Science., Springer Berlin / Heidelberg (2005) 275–283
13. Jolly, M., Grady, L.: 3D general lesion segmentation in CT. In: 5th IEEE International Symposium on Biomedical Imaging: From Nano to Macro, IEEE (2008)
14. Chen, T., Metaxas, D.: A hybrid framework for 3D medical image segmentation. Journal of Medical Image Analysis **9** (December 2005) 547–565
15. Upadhyay, S., Jain, S., Papadakis, M., Azencott, R.: 3D-rigid motion invariant discrimination and classification of 3D-textures. In Papadakis, M., Ville, D.V.D., Goyal, V., eds.: Proc. Wavelets and Sparsity XIV. Volume 8138 of Proceedings SPIE. (2011) 813821
16. Kashyap, R., Chellappa, R.: Estimation and choice of neighbors in spatial-interaction models of images. IEEE Trans. Information Theory **1** (1983) 60–72
17. Ranguelova, E.B.: Segmentation of textured images on three-dimensional lattices. PhD Thesis, University of Dublin, Trinity College (2002)

	Reference Normal	Two fold cross-validation			Leave two out validation		
		Features used			Features used		
		D_M	(RD_0, RD_{-1})	(RD_0, RD_{-1}, D_M)	D_M	(RD_0, RD_{-1})	(RD_0, RD_{-1}, D_M)
L3	N1	73.4	83.4	86.2	67.2	58.3	90.6
	N2	73.6	74.4	71.1	83.3	78.1	49.5
	N3	75.0	82.9	84.7	75.5	78.1	93.2
	N4	69.4	78.2	73.4	49.5	65.6	62.5
	N5	77.0	79.4	79.7	92.2	66.7	93.8
	N6	74.6	81.6	79.7	72.9	67.2	93.8
	N7	76.5	84.2	85.6	97.4	77.1	81.3
	N8	75.1	85.2	82.9	99.5	95.3	85.4
	Average	74.3	81.1	80.4	79.7	73.3	81.3
<i>SVM-Voting</i>	74.4	83.2	83.0	91.1	70.3	91.1	
L4	N1	93.1	71.4	84.9	83.3	56.3	71.4
	N2	89.0	70.4	89.1	73.4	63.0	92.7
	N3	95.2	68.6	90.6	84.4	52.6	87.5
	N4	92.5	70.1	93.0	79.2	76.6	95.8
	N5	89.5	78.0	91.3	83.3	85.4	90.1
	N6	95.0	68.8	90.5	93.8	72.9	92.7
	N7	95.2	74.4	91.2	92.7	69.3	94.8
	N8	95.3	80.0	91.6	97.4	87.5	93.8
	Average	93.1	72.7	90.3	85.9	70.4	89.8
<i>SVM-Voting</i>	93.5	69.7	91.5	90.6	67.2	93.8	
L5	N1	95.0	71.4	93.5	82.8	50.5	91.1
	N2	95.1	70.0	92.0	87.0	66.7	94.8
	N3	95.1	70.3	93.2	78.1	68.8	99.0
	N4	99.2	75.1	95.0	100	59.9	92.2
	N5	95.1	72.1	92.1	79.2	56.8	93.8
	N6	97.5	72.3	92.9	100	76.0	95.8
	N7	96.7	73.7	91.7	99.5	58.9	88.5
	N8	95.0	70.6	93.0	69.3	47.4	99.0
	Average	96.1	71.9	92.9	87.0	60.6	94.3
<i>SVM-Voting</i>	95.0	72.3	93.2	91.1	55.7	95.8	
L6	N1	96.2	91.1	99.6	99.5	100	100
	N2	95.1	74.2	96.8	96.9	81.3	100
	N3	97.9	74.0	98.1	100	80.2	100
	N4	98.3	81.3	98.9	100	75.5	100
	N5	98.4	66.7	95.0	100	80.7	99.5
	N6	95.2	82.2	97.6	96.4	85.9	100
	N7	97.9	81.6	99.9	100	81.3	100
	N8	95.0	70.7	96.4	93.8	51.6	100
	Average	96.7	77.7	97.8	98.3	79.6	99.9
<i>SVM-Voting</i>	95.5	79.8	98.6	100	82.8	100	

Table 2. Continuation of Table 1 to show the classification accuracy obtained from the two experiments for rest of the four patients (L3-L6).